






## Article

# Photocatalytic Organic Contaminant Degradation of Green Synthesized ZrO<sub>2</sub> NPs and Their Antibacterial Activities

Parvathiraja Chelliah <sup>1,\*</sup>, Saikh Mohammad Wabaidur <sup>2</sup>, Hari Prapan Sharma <sup>3</sup>, Hasan Sh. Majdi <sup>4</sup>,  
Drai Ahmed Smaït <sup>5</sup>, Mohammed Ayyed Najm <sup>6</sup>, Amjad Iqbal <sup>7</sup> and Wen-Cheng Lai <sup>8,9,\*</sup>

<sup>1</sup> Department of Physics, Manonmaniam Sundaranar University, Tirunelveli 627012, Tamilnadu, India

<sup>2</sup> Chemistry Department, College of Science, King Saud University, Riyadh 11451, Saudi Arabia

<sup>3</sup> Department of Business Management, GLA University, Mathura 281406, Uttar Pradesh, India

<sup>4</sup> Department of Chemical Engineering and Petroleum Industries, Al-Mustaqbal University College, Babylon 51001, Iraq

<sup>5</sup> Department of Law, The University of Mashreq, Baghdad 11001, Iraq

<sup>6</sup> Faculty of Pharmacy, Al-Rafidain University College, Baghdad 46036, Iraq

<sup>7</sup> Department of Advanced Materials & Technologies, Faculty of Materials Engineering, Silesian University of Technology, 44-100 Gliwice, Poland

<sup>8</sup> Bachelor Program in Industrial Projects, National Yunlin University of Science and Technology, Douliu 640301, Taiwan

<sup>9</sup> Department of Electronic Engineering, National Yunlin University of Science and Technology, Douliu 640301, Taiwan

\* Correspondence: cpdraja1206@gmail.com (P.C.); wenlai@yuntech.edu.tw or wenlai@mail.ntust.edu.tw (W.-C.L.)

**Abstract:** The green synthesis of metal oxide nanoparticles is an efficient, simple, and chemical-free method of producing nanoparticles. The present work reports the synthesis of *Murraya koenigii*-mediated ZrO<sub>2</sub> nanoparticles (ZrO<sub>2</sub> NPs) and their applications as a photocatalyst and antibacterial agent. Capping and stabilization of metal oxide nanoparticles were achieved by using *Murraya koenigii* leaf extract. The optical, structural, and morphological valance of the ZrO<sub>2</sub> NPs were characterized using UV-DRS, FTIR, XRD, and FESEM with EDX, TEM, and XPS. An XRD analysis determined that ZrO<sub>2</sub> NPs have a monoclinic structure and a crystallite size of 24 nm. TEM and FESEM morphological images confirm the spherical nature of ZrO<sub>2</sub> NPs, and their distributions on surfaces show lower agglomerations. ZrO<sub>2</sub> NPs showed high optical absorbance in the UV region and a wide bandgap indicating surface oxygen vacancies and charge carriers. The presence of Zr and O elements and their O=Zr=O bonds was categorized using EDX and FTIR spectroscopy. The plant molecules' interface, bonding, binding energy, and their existence on the surface of ZrO<sub>2</sub> NPs were established from XPS analysis. The photocatalytic degradation of methylene blue using ZrO<sub>2</sub> NPs was examined under visible light irradiation. The 94% degradation of toxic MB dye was achieved within 20 min. The antibacterial inhibition of ZrO<sub>2</sub> NPs was tested against *S. aureus* and *E. coli* pathogens. Applications of bio-synthesized ZrO<sub>2</sub> NPs including organic substance removal, pathogenic inhibitor development, catalysis, optical, and biomedical development were explored.

**Keywords:** ZrO<sub>2</sub> NPs; green synthesis; photocatalysis; bacterial activity; *Murraya koenigii*



**Citation:** Chelliah, P.; Wabaidur, S.M.; Sharma, H.P.; Majdi, H.S.; Smaït, D.A.; Najm, M.A.; Iqbal, A.; Lai, W.-C. Photocatalytic Organic Contaminant Degradation of Green Synthesized ZrO<sub>2</sub> NPs and Their Antibacterial Activities. *Separations* **2023**, *10*, 156. <https://doi.org/10.3390/separations10030156>

Academic Editors: Mohamed Nageeb Rashed and Mohamed Farid Cheira

Received: 22 January 2023

Revised: 16 February 2023

Accepted: 21 February 2023

Published: 24 February 2023



**Copyright:** © 2023 by the authors. Licensee MDPI, Basel, Switzerland. This article is an open access article distributed under the terms and conditions of the Creative Commons Attribution (CC BY) license (<https://creativecommons.org/licenses/by/4.0/>).

## 1. Introduction

Ecological contamination and climate modifications are promoting a major impact on the world and demotivating the economy and healthy life for all [1–3]. The contamination of water and its associated issues constitute one of the most serious problems facing humans today. The issue of water contamination can be addressed by using different techniques. Various methods are available to eradicate and remediate polluted water sources [4–7]. Nanotechnology is one of the more potent remediation technologies compared to other methods because of the smaller size, which helps the particles to easily penetrate the polluted system and react. Recently, metal oxide nanoparticles have been paid more attention in the fields

of bio-activity, sensors, photocatalysis, electrocatalysis, adsorbents, etc. [8–12]. ZrO<sub>2</sub> NPs have excellent mechanical, optical, electrical, biocompatible, and catalytic stability, making them suitable for a variety of catalytic, biomedical, and sensor applications. Three different phases (cubic, monoclinic, and tetragonal) of ZrO<sub>2</sub> NPs are obtained in the output of ZrO<sub>2</sub> NPs. In addition, p-type ZrO<sub>2</sub> NPs have exhibited a high bandgap, low phonon energy, high adsorption in the UV region, reduction, and oxidation potential due to their acidic and basic nature provoking hydroxyl and superoxide ions [13,14]. Numerous techniques exist for the synthesis of ZrO<sub>2</sub> NPs, such as coprecipitation, hydrothermal, laser ablation, photochemical, sonochemical, and microwave-assisted routes. These techniques are produced by the multiple phases of ZrO<sub>2</sub> NPs. The electron trapping and oxygen vacancies on the surfaces of the ZrO<sub>2</sub> NPs vary according to the crystal structure. The Green Chemistry Route has always emphasized sustainability and developed noxious-free synthesis techniques [15–22]. Moreover, noxious-free synthesis reduces the negative impact on the environment. Plant-mediated synthesis is gaining much attention due to its bio-molecule reduction, stabilization, and capping activities [23–25]. Through the combination of green chemistry and nanotechnology, chemical-free synthesis was introduced, and nucleation growth, size, shape, and charge transfer were tuned. The reduction of metal ions and electron transfer from different bands are determined from the bio-compounds [26]. The plant-extract-mediated nanoparticle synthesis method accelerates bacterial inhibition due to microbial resistance, which reacts with the bacterial system [27]. In the present work, three important aspects of the synthesized nanoparticles are discussed: (i) The green chemical method of nanoparticle production, (ii) photocatalytic dye degradation, and (iii) microbial inactivation. The *Murraya koenigii* plant leaves contain various bio-chemicals, namely, inulool, elemol, geranyl acetate, myrcene, ocimene, terpinene, and quercetin [28–30]. These are involved in the reactions of bio-capping, bio-chelating, bio-reduction, bio-encapsulation, and bio-stabilization of nanoparticles. Dyes are very applicable as major elements for color-related industries such as paint, textile, leather, and printing. The release of dyestuffs comprising colors and highly stable non-degradable organic substances is a major concern for the environment. Many dyes are used in these industries such as methyl violet, methyl red, methylene blue (MB), congo red, and rhodamine B [31–35]. Among the above-mentioned dyes, MB is regularly used in day-to-day life and in textile and various other industries. Several methods are accessible for the removal of dye compounds from surfaces. Photocatalysis is an easy and abundant technique to eradicate organic compounds with the help of various light sources. A visible light source is a renewable energy source available all over the world. Dye pollutants modify the origin of all water sources and disrupt the ecological domains. The discharge of MB dye effluents creates mutagenic and carcinogenic diseases. Bacterial limitations on the microorganisms induce a toxic effect on the environment and produce contagious diseases on the surface [36–41]. *E. coli* and *S. aureus* bacterial strains are very harmful food-borne and human-borne pathogens and initiate various infections at intestinal and gastroenteritis sites. All over the world, these harmful bacterial strains increase the death rate every year. Considering the harmful effects of the dye and two different human-borne pathogens, bio-synthesized ZrO<sub>2</sub> NPs were investigated in the removal of such adverse effects on humanity.

## 2. Materials and Methods

ZrO<sub>2</sub> NPs were formulated from analytical reagent (AR)-grade Zirconium nitrate (Zr(NO<sub>3</sub>)<sub>4</sub>, 99.9% purity) and *Murraya koenigii* plant extract. Methylene blue (C<sub>16</sub>H<sub>18</sub>ClN<sub>3</sub>S; 99.9% purity) was obtained from HiMedia, India. The procured chemicals were used without any modifications. The reaction and solutions were created using double-distilled water.

## 3. Preparation of the Plant Extract

Green and fresh leaves of *Murraya koenigii* were bought from Bengaluru, Karnataka, India, and cleaned with tap water. The washed leaves were soaked in double-distilled water, and a mortar was used to crush the leaves. White cotton cloth was used to filter the dark green plant extract, and the obtained solution was dissolved in 100 mL of

double-distilled (DD) water. The mixed leaf extract of *Murraya koenigii* was deposited for future characterizations.

#### 4. Biosynthesis of ZrO<sub>2</sub> NPs

Biosynthesized ZrO<sub>2</sub> NPs were formulated using a 0.1 M Zr(NO<sub>3</sub>)<sub>4</sub> metal nitrate solution mixed with 10 mL of the *Murraya koenigii* plant extract using a magnetic stirrer (60 min). The combination of metal nitrate and *Murraya koenigii* plant leaf extract dissolutions was used to construct the ZrO<sub>2</sub> NPs. The bio-extract of *Murraya koenigii* reacts with the metal nitrate solution and emanates a milky white-colored solution. The white-colored solutions deliver the nuclei formation of ZrO<sub>2</sub> NPs' atomic layers. The white-colored ZrO<sub>2</sub> NPs were processed by repeated centrifugation at 10,000 rpm for 15 min, and the obtained precipitate was washed with double-distilled water. Finally, the collected white precipitate was dried for 1 h at 100 degrees Celsius, and the white powder of ZrO<sub>2</sub> NPs was collected and stored for further evaluation.

#### 5. Characterization Methods

The crystalline material and phase structure were analyzed by an X-ray diffractometer (X-Pert Pro-Cu K<sub>α</sub> radiation  $-1.5405 \text{ \AA}$ ; 60 kV and 40 mA;  $2\theta$  limit of  $20-80^\circ$ ). The surface functional groups of the ZrO<sub>2</sub> NPs were captured using FTIR (Perkin Elmer  $\lambda = 4000 \text{ cm}^{-1}$  to  $400 \text{ cm}^{-1}$ ). The optical defects and their analysis were captured using UV-DRS (Shimadzu  $\lambda = 200$  to  $800 \text{ nm}$ ). The morphological beings and their existing surface elements were derived from FE-SEM (FE-SEM, Ultra 55, Zeiss, Jena, Germany) with EDX (EDS, X-max, Oxford Instruments, Wycombe, UK) analysis, and their surface inner objectives were determined using TEM (Titan) analysis. The material binding and bonding between the materials and bio-reductant were observed using X-ray photoelectron spectroscopy (XPS, PHI 5000 Versa Probe III, Physical Electronics, Chanhassen, MN, USA).

#### 6. Photocatalytic Dye Degradation

The visible-light-driven photocatalytic dye degradation efficiency of synthesized nanoparticles was inspected by determining the methylene blue (MB) dye degradation. Primarily, 10 mg of synthesized nanoparticles were well dispersed in a 10 ppm MB solution using the ultrasonication method. The ultrasonicated solution was placed in a dark chamber for 30 min and stirred with the help of a magnetic stirrer. The absence of light created an equilibrium condition. After that, the samples were irradiated by visible light. The visible light source was a Xe lamp ( $\lambda = 400 \text{ nm}$ ), and the distance between the samples was 8 cm. At periodic intervals, the irradiated samples were withdrawn and centrifuged (1000 rpm) to eliminate the nanoparticles. Finally, the collected dye solutions were measured by a UV-Visible spectrophotometer. The dissociated MB dye concentrations were observed at an absorbance of 665 nm. The active species of the photocatalyst was analyzed using the quenching measurement, which can be used to determine the free radicals, holes, and superoxides. The quenchers of quenchers (triethanolamine (TEOA), (p-benzoquinone (BQ), and (isopropyl alcohol (IPA)) are used at a 1 mmol/L concentration to determine the quencher analysis, and their readings were taken using UV-Visible spectroscopy [42].

The dye degradation efficiency against the nanoparticles was calculated by the following formula:

$$\text{MB dye degradation efficiency} = ((C - C_t)/C) * 100$$

where C is the initial dye concentration at zero time and C<sub>t</sub> is the dye concentration at periodic time intervals.

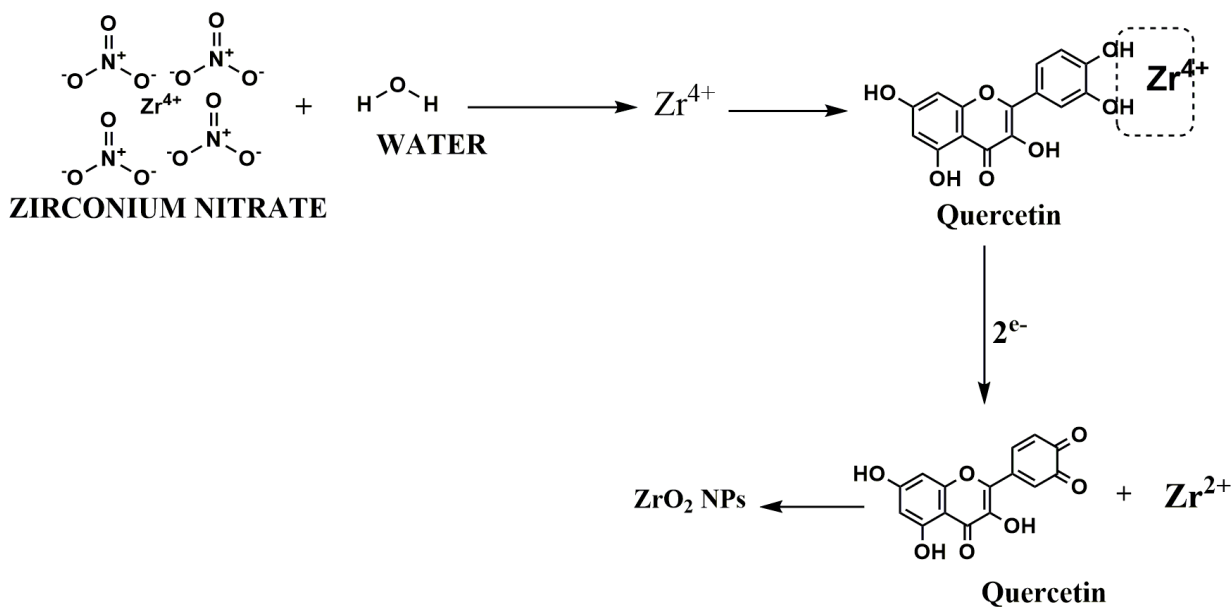
#### 7. Antibacterial Activity

The antibacterial study of the synthesized nanoparticles against *Staphylococcus aureus* (ATTC-6538) and *Escherichia coli* (ATTC-8739) were evaluated by the disc diffusion method. The solidification process was carried out was nutrient agar, and sterilized Petri plates were

filled with nutrient agar. The solidified plates were spread with a fresh bacterial culture. The four different concentrations (10, 20, 50, and 100 µg) of synthesized nanoparticles were loaded by 6 mm paper discs. The nanoparticle-loaded plates were incubated at 36 °C for 24 h. Finally, the incubated plates were produced in the inhibition zones. The observed bacterial activities were compared by standard amikacin discs. The inhibited zone was measured on the mm scale. The zone of inhibitions displays the effect of bacterial inactivity of synthesized nanoparticles [41,42].

### 8. Reaction Mechanism of Zirconium Oxide Nanoparticles

Zirconium oxide nanoparticles were synthesized from  $Zr(NO_3)_4$  using the leaf extract of *Murraya koenigii*. The *Murraya koenigii* green leaves have shown remarkable biological properties including antioxidant, antibacterial, antifungal, anti-inflammatory, and anti-cancer activities [43]. Quercetin is one of the most important flavonoids in the leaf extract of *M. koenigii* [44]. The reported findings [45] indicate that the presence of quercetin in the leaf extract of *M. koenigii* might act as a reducing/stabilizing agent in the production of gold nanoparticles. In the present work, the *M. koenigii* leaf extract of the quercetin compound may donate an electron to zirconium ions ( $Zr^{4+}$ ) and reduce them to  $ZrO_2$  NPs. The developed electrons from quercetin compounds form the interface between metal and oxygen materials. The metal oxide nanoparticles using the *M. koenigii* formation mechanism are presented in Scheme 1.



**Scheme 1.** Possible mechanism for the synthesis of  $ZrO_2$  NPs using the *M. koenigii* leaf extract.

## 9. Result and Discussions

### 9.1. XRD Analysis

The X-ray diffractogram pattern of the biosynthesized  $ZrO_2$  NPs is presented in Figure 1. The diffraction peaks at  $2\theta = 17.48^\circ, 24.17^\circ, 24.47^\circ, 28.12^\circ, 31.37^\circ, 34.13^\circ, 35.42^\circ, 38.58^\circ, 40.03^\circ, 44.77^\circ, 49.29^\circ, 49.99^\circ, 54.03^\circ, 57.48^\circ, 55.41^\circ, 60.02^\circ, 62.99^\circ,$  and  $65.54^\circ$  can be assigned to the (001), (110), (001), (−111), (111), (200), (002), (120), (−112), (211), (220), (022), (310), (131), (113), and (222) planes of the monoclinic structure of the  $ZrO_2$  NPs, which aptly matches previously reported work and the standard JCPDS File No: 37-1484 [46,47]. There are no diffraction peaks of any other crystal phases observed in any of the samples, indicating that they are all pure monoclinic  $ZrO_2$  NPs. The crystalline nature of the nanoparticles is influenced by the size and particle expression over the material surface, and they may be applicable in various applications. The Debye–Scherrer formula [48] was used to calculate the crystallite size of the nanoparticles, which was found to be 24 nm.

Phases without any other impurities and narrow crystallite sizes of ZrO<sub>2</sub> NPs provided better crystallinity and structural stability.

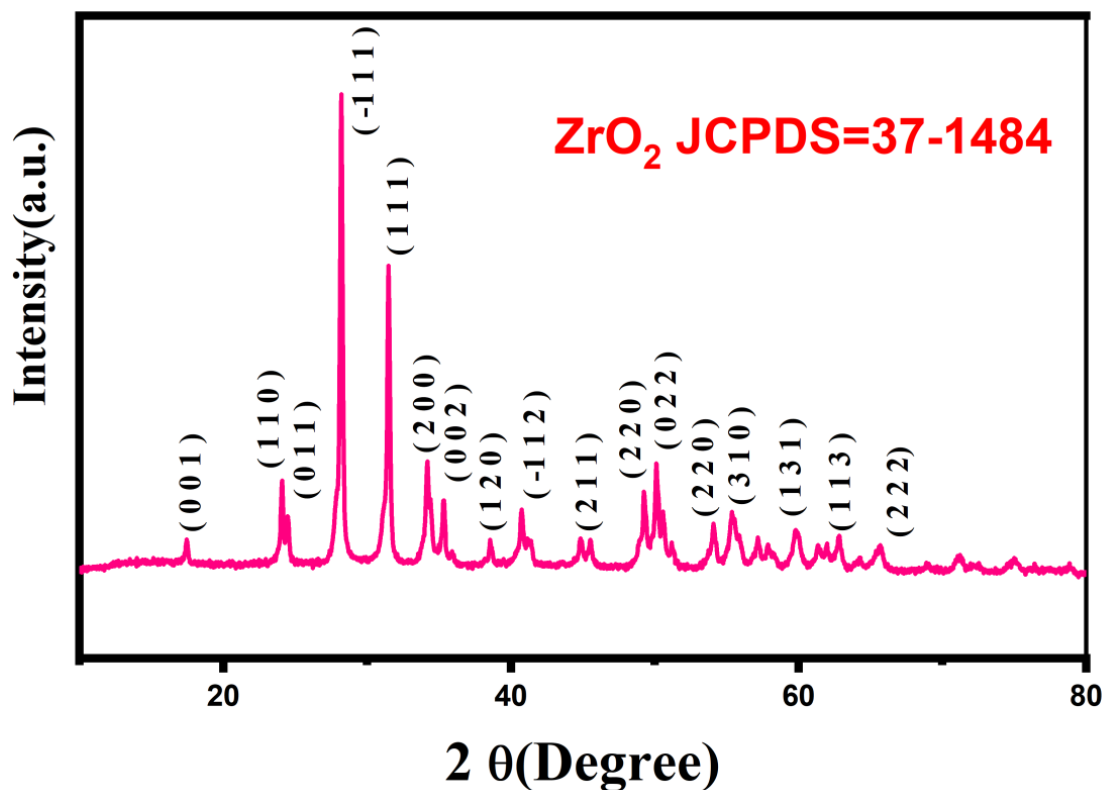


**Figure 1.** XRD pattern of ZrO<sub>2</sub> NPs.

### 9.2. FTIR Analysis

The biosynthesized ZrO<sub>2</sub> NPs were analyzed with Fourier transform infrared spectroscopy (FTIR) and are shown in Figure 2. The OH-stretching on the outer surface of the nanoparticles was represented by the presence of a peak at 3055 cm<sup>-1</sup> [49,50]. The aromatic amine and carbon-associated peaks were located at 1629 cm<sup>-1</sup>, 1301 cm<sup>-1</sup>, and 1032 cm<sup>-1</sup>, which indicates the bending vibrations of the C-H bond [50–53]. The carbon peaks arose from plant bio-compounds. The bonding of O=Zr=O and the metal–oxygen interface was confirmed in the synthesized ZrO<sub>2</sub> NPs by the bands of 813 cm<sup>-1</sup> and 734 cm<sup>-1</sup> [53–55]. The obtained FTIR results of synthesized ZrO<sub>2</sub> NPs delivered the reduction and lattice oxygen stabilization process with the help of bio-derivatives.

### 9.3. UV-DRS Analysis

The UV-DRS absorbance spectrum and bandgap plot of biosynthesized ZrO<sub>2</sub> NPs are displayed in Figure 3. Figure 3a demonstrates the optical absorption of ZrO<sub>2</sub> NPs at 260 nm. These spectral activities determine the better photocatalytic degradation abilities over the target organic substances. The formation of the ZrO<sub>2</sub> nanostructure was evident from the (Zr<sup>4+</sup> and O<sup>2-</sup>) reduction and stabilization [56]. Kubelka–Munk relations are helpful to determine the optical nature, and their values are presented in Figure 3b. The bandgap is 4.7 eV, which constitutes a wide bandgap and time-suspended e–h pair activity [57,58]. The oxygen vacancy increased the charge carrier generation, which enhanced the dissociation of pollutants from aquatic surfaces. The plant molecule interface between the metal sources may form the metal-oxide nanostructures on the surface. Based on the UV-DRS results of biosynthesized ZrO<sub>2</sub> NPs, the nanoparticles' bandgap determined the light absorption enhancement and active site advancement on the catalyst surfaces, which provokes radical activity and super oxide productions.

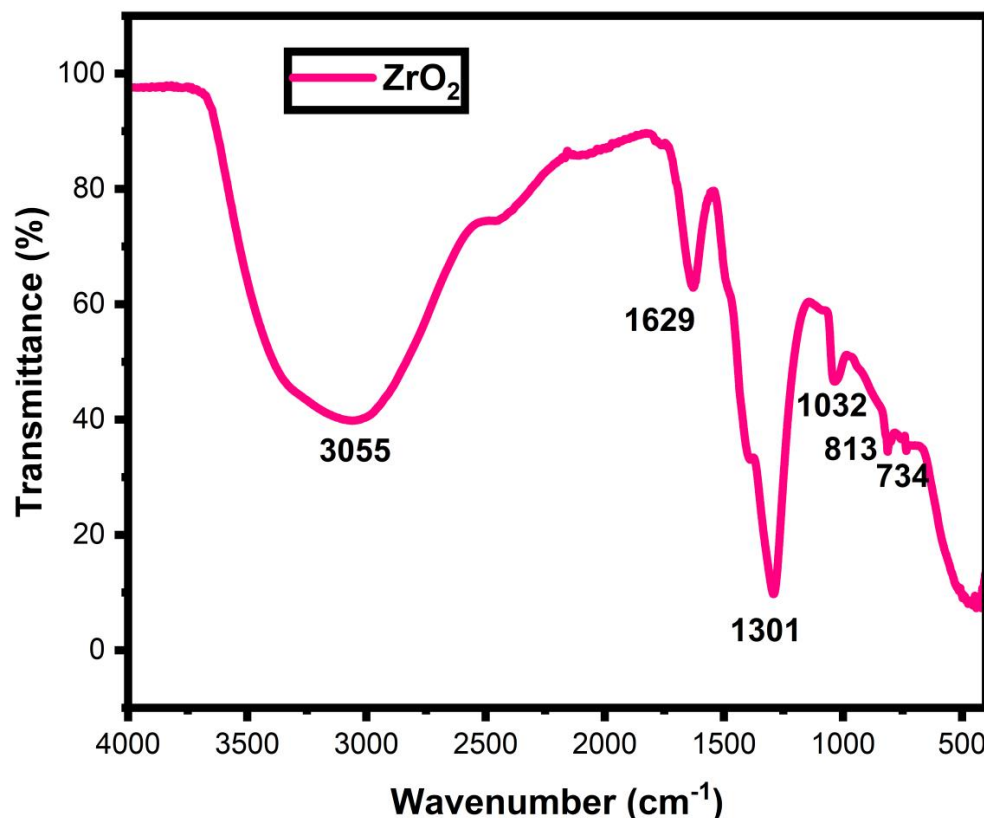


Figure 2. FTIR spectrum of biosynthesized ZrO<sub>2</sub> NPs.

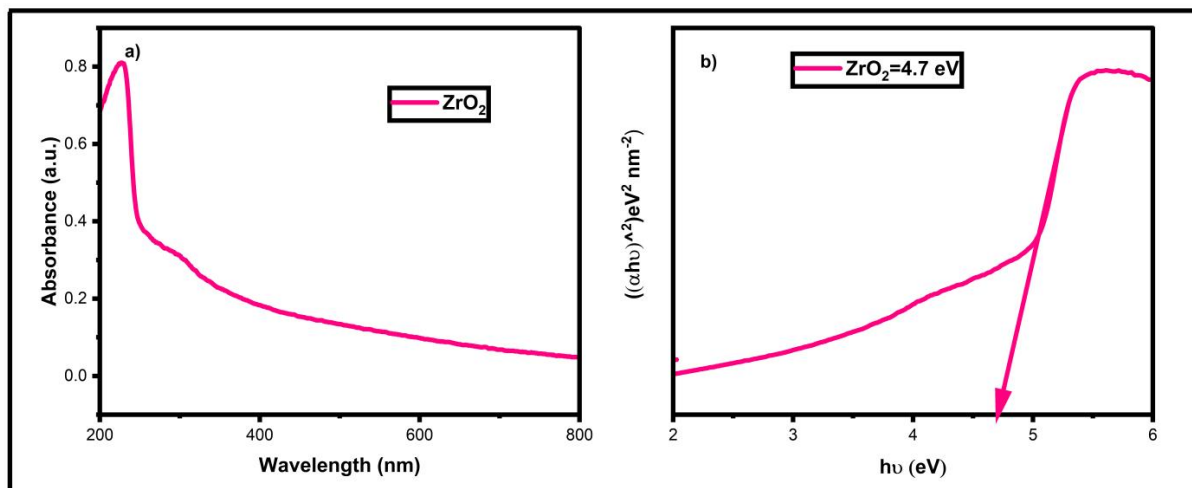
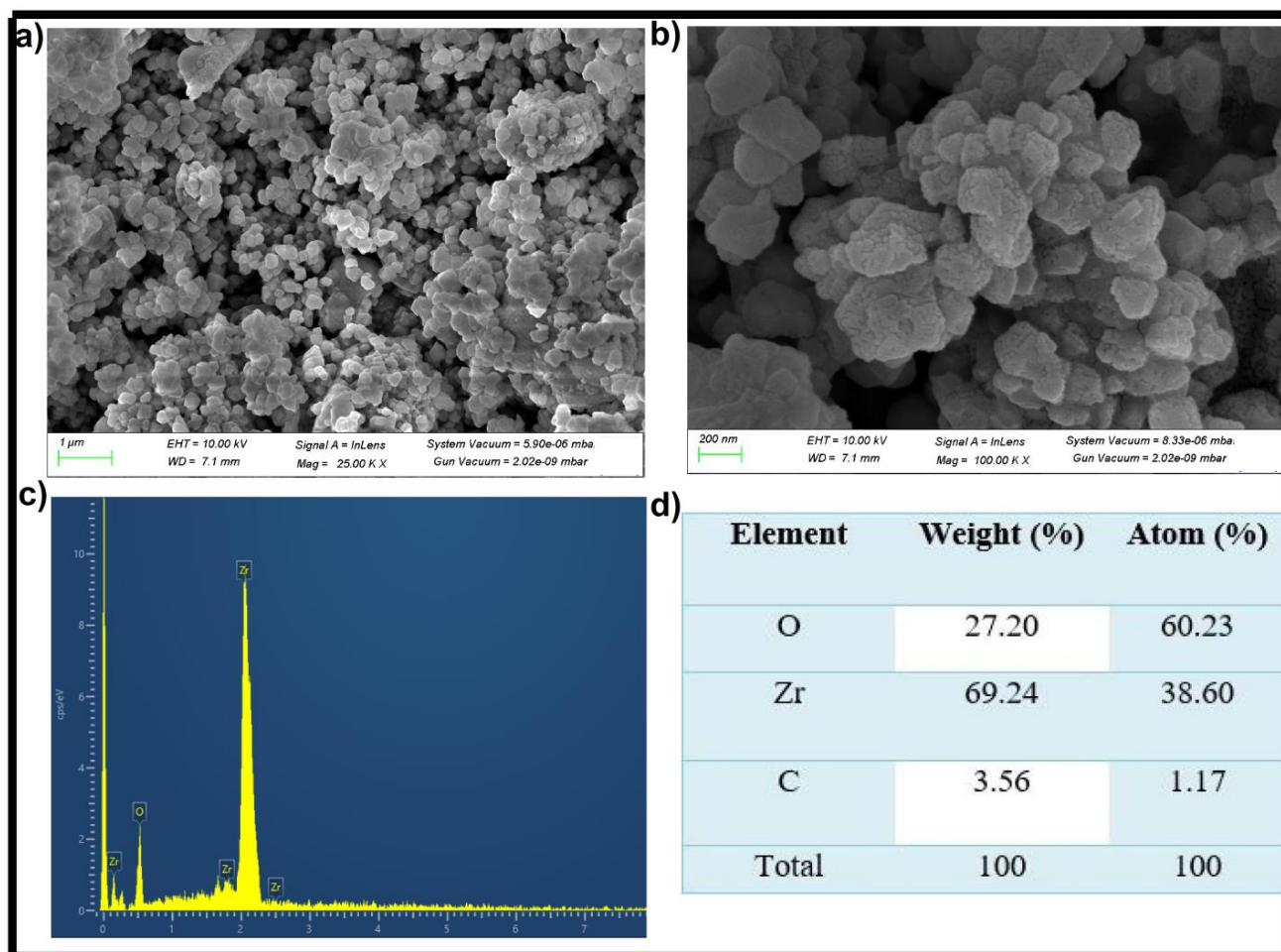


Figure 3. UV-DRS absorbance spectrum (a) and bandgap plot (b) of biosynthesized ZrO<sub>2</sub> NPs.

#### 9.4. FESEM with EDX Analysis

The shape and material compositions were detected using FESEM with EDX analysis. Figure 4a,b depicts the spherical shape. Most of the particles attained a spherical shape, while other particles obtained a combined spherical shape. Particles are found to be eventually distributed over the surface. The spherical shape of nanoparticles caused the enhanced degradation efficiency towards the noxious organic substances [59,60]. The material composition of ZrO<sub>2</sub> NPs is depicted in Figure 4c,d. Lattice oxygen was attracted and combined by zirconium metals, which induces metal–oxygen bonding by using plant molecules [61]. Oxygen (27%) attracted 69% zirconium to form the ZrO<sub>2</sub> NPs. The lattice oxygen with zirconium metal created the spherical shape, which can demotivate the spreading of toxic compounds due to the existence of Zr<sup>4+</sup> and O<sup>2-</sup>. The unassigned peaks

are carbon materials, which are derived from plant bio-compounds and carbon tap. The 3.5% of carbon elements obtained was well established in the FTIR section.



**Figure 4.** FE-SEM images (a,b), EDX spectrum (c), and table (d) of biosynthesized ZrO<sub>2</sub> NPs.

### 9.5. TEM Analysis

The surface morphological presence, particle distributions, and size of ZrO<sub>2</sub> NPs were determined using TEM analysis (Figure 5). The synthesized nanoparticles were distributed consistently, and their size was found to be 27 nm. The plant bio-nutrients developed the equally phased spherical nanoparticles on the surface, and their lattice arrangement over the Zr and O atoms produced the poly-dispersity in biosynthesized ZrO<sub>2</sub> NPs [62,63]. The spherical shape is more unique than other shapes of nanoparticles because of their large surface area and high penetrating ability in bacterial domains. Moreover, spherical-shaped nanoparticles are highly appreciable in biomedical applications [64,65].

### 9.6. XPS Analysis

The chemical presence, composition, and valency of biosynthesized ZrO<sub>2</sub> NPs were determined using XPS analysis (Figure 6a–d). The wide spectrum comprises Zr-3d, O-1s, and C-1s elements belonging to the biosynthesized ZrO<sub>2</sub> NPs. The Zr spectrum emanates in a 3d state, and their binding energies were 181.8 eV (Zr-3d<sub>5/2</sub>) and 184.2 eV (Zr-3d<sub>3/2</sub>). The obtained Zr spectrum binding energies aptly matched previously reported work [66–68]. The Zr peaks denoted the metal’s existence, and there were no other metals involved in the reaction. The exhibited oxygen spectrum displayed at 531 eV is in the O-1s state. Zr<sup>4+</sup> and O<sup>2-</sup> formations and their interactions created the ZrO<sub>2</sub> NPs [69]. The carbon peaks were attributed to the plant extract, and their plant bio-chemicals were used to modify

the valence-free metal and lattice oxygen stabilization with metal. The above-mentioned actions were displayed at the binding energy of 233 eV to 238 eV and represent the C-C, C-O, and C=O bonds, and their bonding was confirmed by FTIR analysis [70,71].

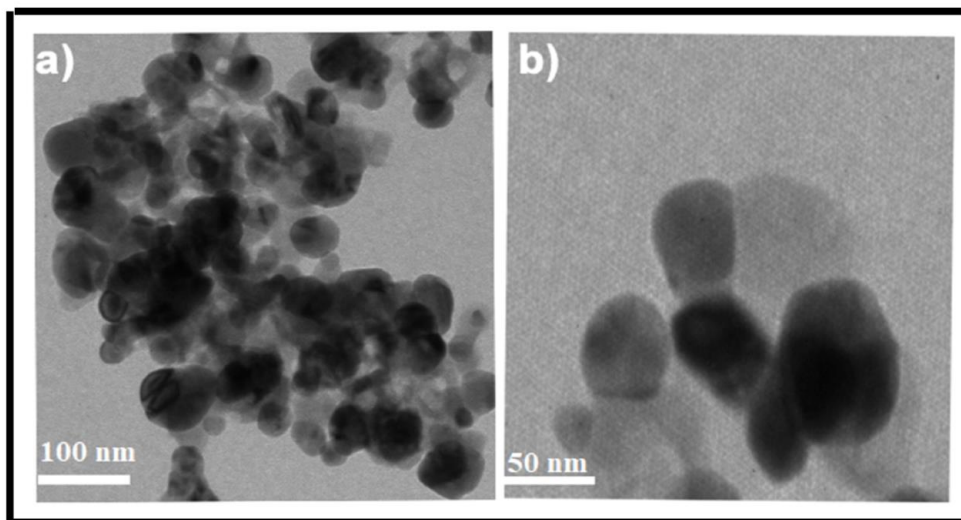


Figure 5. TEM images (a,b) of biosynthesized ZrO<sub>2</sub> NPs.

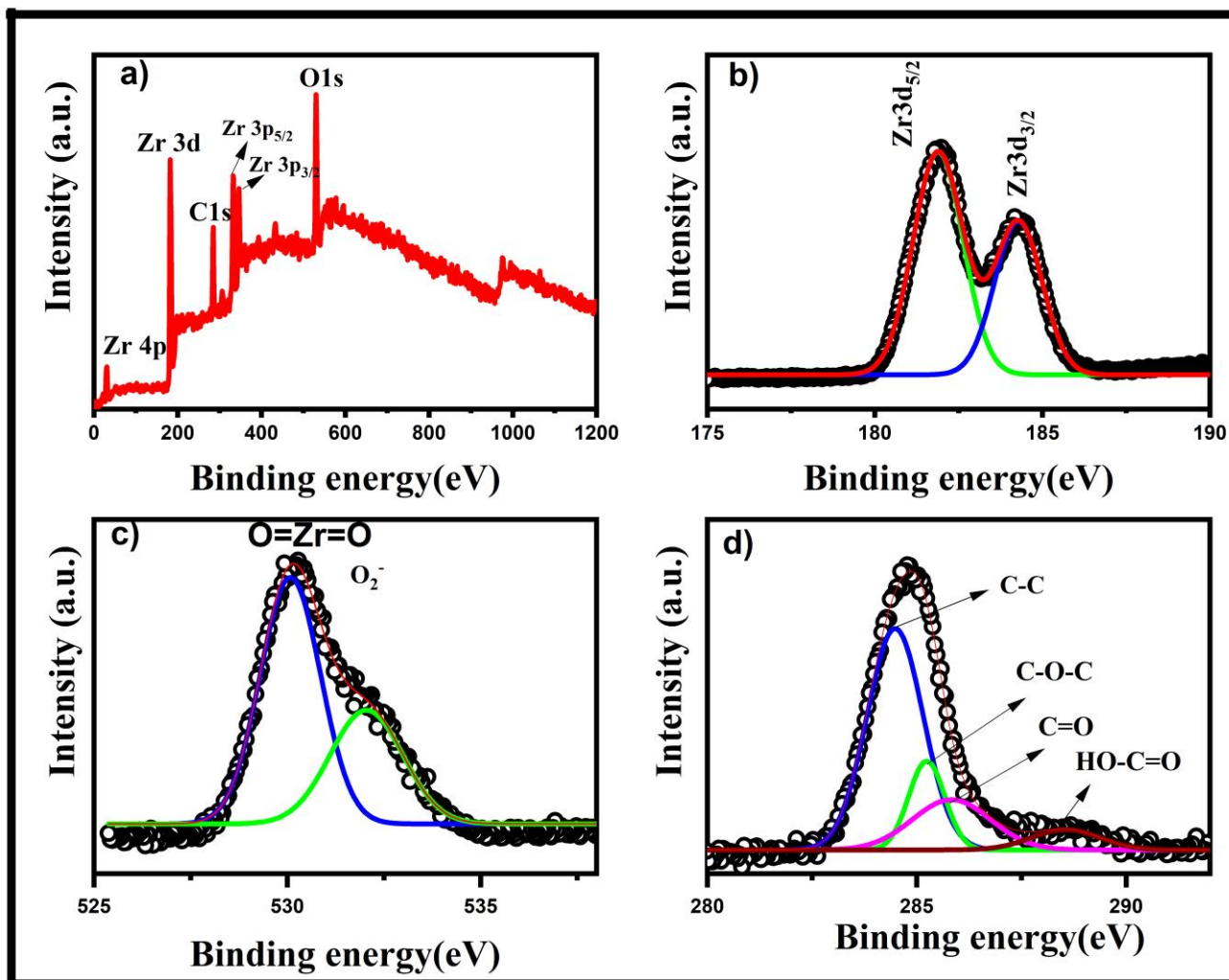


Figure 6. XPS wide (a), Zr-2p (b), O-1s (c), and C-1s (d) spectra of biosynthesized ZrO<sub>2</sub> NPs.



### 10. Photocatalytic Dye Degradation

The photocatalytic activity of synthesized ZrO<sub>2</sub> NPs was evaluated by estimating the degradation of MB at 664 nm as shown in Figure 7. Under simulated visible light irradiation, the absorption of the MB dye solution in the presence of the ZrO<sub>2</sub> photocatalyst decreases with increasing irradiation time. Visible light sources are abundant light, and their absorption range is high and does not require high energy. Without nanoparticles, the dye degradation is 8%, as the electron excitation in light irradiation is very low. The electron migration on the surface reduced the dye bonding. During the excitation, in the presence of nanoparticles, the active sites are very high compared to nanoparticle samples without light irradiation [72,73]. In the photocatalysis reaction on the photocatalyst material, electrons were excited to the conduction band from the valence band. Furthermore, the same number of holes was created in the valence band. Then the conduction-band electrons and the trapped electrons moved together to the surface of the photocatalyst and were trapped by the oxygen vacancies present on the surface [74–77]. The oxygen vacancies trap the O<sub>2</sub> molecules and this led to the formation of superoxide radicals (O<sub>2</sub><sup>-•</sup>). Meanwhile, the oxygen molecules present in the MB dye solution interacted with the surface oxygen vacancies and further changed into superoxide radicals [78–82]. Similarly, holes were trapped by water (H<sub>2</sub>O) molecules or OH<sup>-</sup> groups to create hydroxyl radicals (OH<sup>•-</sup>). Finally, the generated radicals interact with the pollutant and effectively degrade the target dye. The complete mechanism for the degradation of MB dye can be understood by the following chemical reaction, which shows a graph of ln(C<sub>0</sub>/C) vs. time (min). The kinetic study infers the order of the reaction. The graph depicts a straight line with a positive slope and a rate constant of 0.06272 min<sup>-1</sup> for ZrO<sub>2</sub> NPs. The ZrO<sub>2</sub> photocatalyst showed 94% degradation of MB after 20 min of the reaction. Figure 7d shows a graph of ln(C<sub>t</sub>/C<sub>0</sub>) vs. time (min). The kinetic study infers the order of the reaction. The mechanism of photocatalysis is shown in Figure 7d and their equations are shown in (1)–(6).



There are many factors and reaction output conditions such as size, shape, reductions, pH, temperature, and release of ions that determine the degradation performance of nanomaterials. Different carbon source dopant materials provide better catalytic activity against the indigo carmine dye [83]. The high surface area and narrow crystallite sizes of the ZrO<sub>2</sub> NPs exhibited enhanced degradation activities against the various dyes [84–88]. Scavenging radicals and superoxides are responsible for promoting the highest degradation ability towards the organic dye compounds [85–88]. Visible light and UV light irradiations induced charge production and electron trapping on the semiconductor nanoparticles' surface. Visible light shows a very low production of radical scavengers compared to UV light irradiation [85–91]. The quenching experiment is displayed in Figure 8. The ZrO<sub>2</sub> catalyst degradation is 94%, and their degradation is compared with quenchers. The hole degradation is higher than superoxides and hydroxides, which was measured using TEOA (77%), BQ (49%), and TPA (26%). The radical scavengers influenced the rate of degradation against the organic substances. Based on the above-mentioned table, the synthesized NPs are found to be better photocatalysts of the wastewater process. The ZrO<sub>2</sub> NPs were found to be the best catalyst compared to the other listed materials in Table 1.

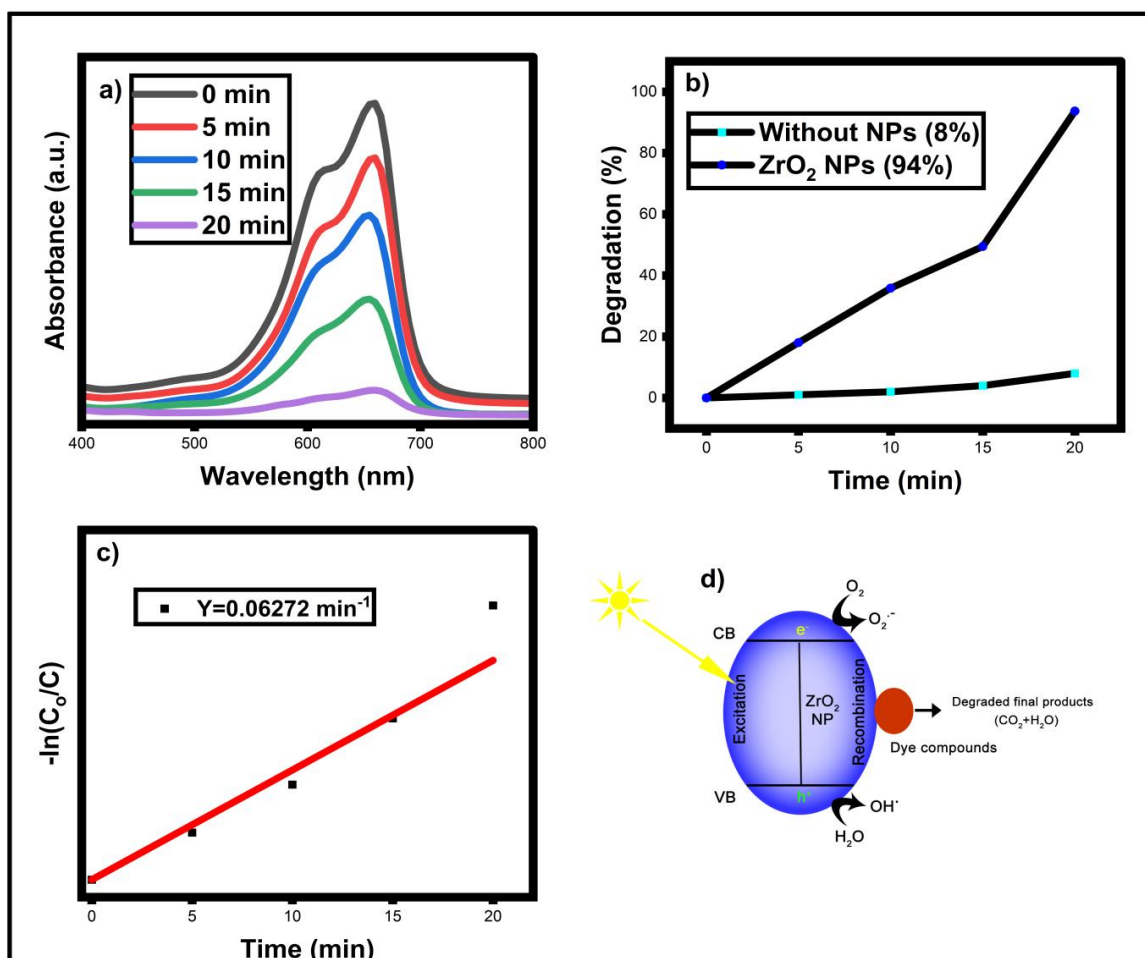


Figure 7. Photocatalytic degradation absorbance spectrum (a), degradation efficiency spectrum (b), pseudo-first-order kinetic spectrum (c), and degradation mechanism (d) of biosynthesized  $ZrO_2$  NPs.

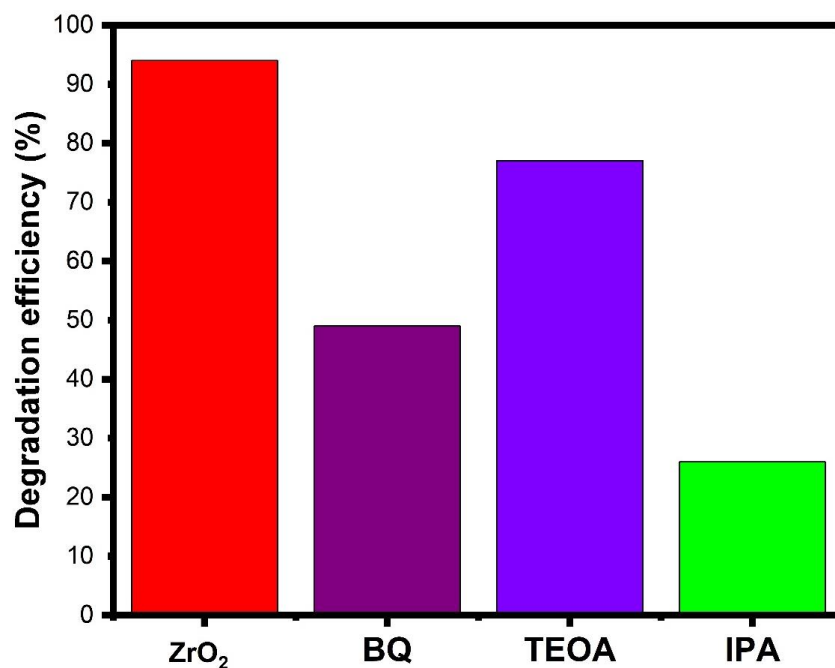


Figure 8. Quenching experiment.

**Table 1.** Photocatalytic dye degradation comparison table of ZrO<sub>2</sub> NPs.

S.No	Sample	Dye	Dye Conc.	Dosage	Degradation	Ref
1.	Eu,C,N,S-doped ZrO <sub>2</sub>	Indigo Carmine	20 mg/L	100 mg	100%	[83]
2.	ZrO <sub>2</sub>	(MO), (MB), (CR), (MG)	10 mg/L	10 mg L <sup>-1</sup>	80%, 92%, 87% and 100%	[84]
3.	ZrO <sub>2</sub>	RY			96.8%	[85]
4.	ZrO <sub>2</sub>	MO	50 ppm	50 mg	99%	[86]
5.	ZrO <sub>2</sub>	MB	20 ppm	60 mg	97	[87]
6.	ZrO <sub>2</sub>	AY	10 mg/L	0.1 g	84.04%	[88]
7.	ZrO <sub>2</sub>	MB and RB	1 mg/L	30 mg	99% and 90%	[89]
8.	ZrO <sub>2</sub>	MO	10 mg/L	100 mg	95%	[90]
9.	ZrO <sub>2</sub>	MO		10 mg	59.4	[91]
10.	ZrO <sub>2</sub>	MB	10 ppm	10 mg	94	Present work

### 11. Antibacterial Activity

The NPs were examined using *Staphylococcus aureus* (gram-positive) and *Escherichia coli* (gram-negative) through the disc diffusion method. The antibacterial zone of inhibition of NPs is demonstrated in Figure 9. Plant-extract-associated ZrO<sub>2</sub> NPs exhibited the highest inhibition against various concentrations. *S. aureus* bacterial sensitivity of green-assisted ZrO<sub>2</sub> NPs is much higher than *E. coli*. The release of Zr<sup>4+</sup> ions controls the bacterial spread and growth of *S. aureus* and *E. coli*. The obtained bacterial inhibition values are enhanced by the amikacin antibiotic disc. The reaction, admission, and interface of the nanoparticles to the bacterial strains determine bacterial growth and death [92–95]. Cell wall membrane leaks were attained from the release of Zr<sup>4+</sup> ions. The plant extract combination on the ZrO<sub>2</sub> NPs increased the radical production and improved the reactive oxygen species (ROS). The admitted metal ions in the bacterial structure promote the electrostatic interaction and lead to ROS production of ZrO<sub>2</sub> NPs [96–101]. Moreover, the dissolution of metal ions and lattice oxygens is derived from the deactivation state of DNA and protein molecules. DNA and protein damage in the bacterial system cut off the food and communications systems, which leads to cell death.

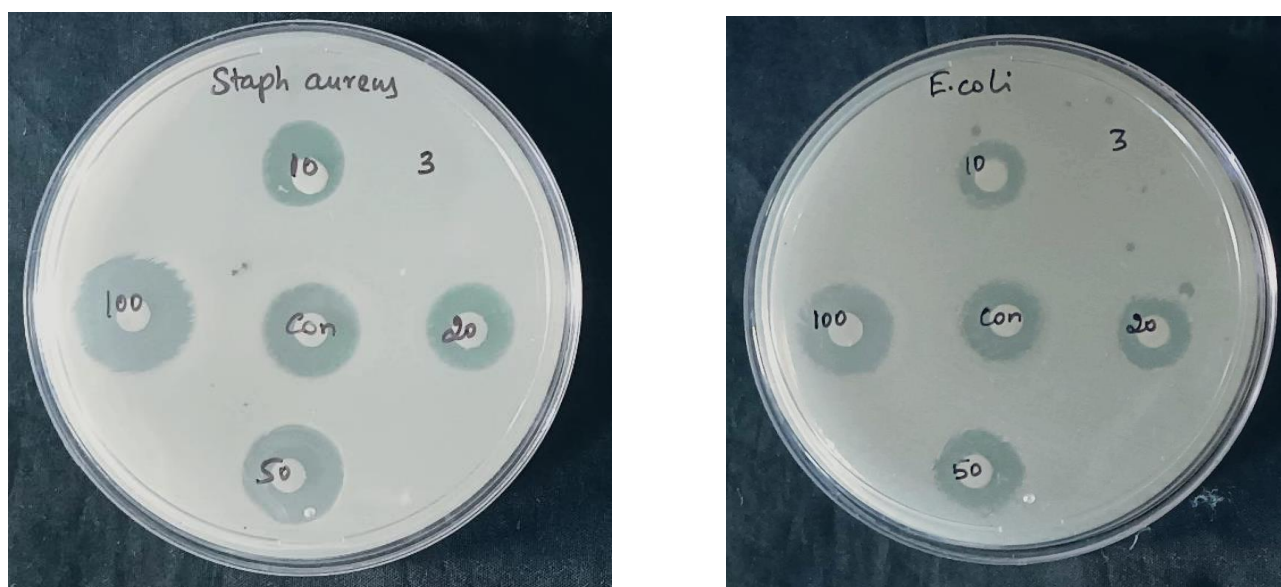


**Figure 9.** Antibacterial activity of biosynthesized ZrO<sub>2</sub> NPs against *S. aureus* and *E. coli*.

### 12. Conclusions

Bio-extracts of *Murraya koenigii* leaf were used to achieve the formation of ZrO<sub>2</sub> NPs. The monoclinic structure, spherical shape, and wide bandgap (4.7 eV) of ZrO<sub>2</sub>

NPs demonstrated enhanced structural, optical, and crystalline properties. Bio-mediated nanoparticle synthesis was proven to be a very esteemed production technique compared to other methods. The plant extract played a very prominent role in nanoparticle production. The *Murraya koenigii* leaf extract is attributed to many roles, including the bio-reduction, stabilization, and bio-capping of ZrO<sub>2</sub> NPs. The wide bandgap, lowest size, and spherical morphology of ZrO<sub>2</sub> NPs concluded the electron trapping and radical generations over the surfaces. The synergetic interactions of *Murraya koenigii* and strontium source materials produced bio-encapsulated ZrO<sub>2</sub> NPs. The biosynthesized ZrO<sub>2</sub> NPs were examined against toxic dye pollutants and two different human-borne pathogens. The visible light irradiation of ZrO<sub>2</sub> NPs showed greater photocatalytic degradation of MB dye pollutants. The bacterial deactivations of ZrO<sub>2</sub> NPs exhibited better results against *E.coli*. The ROS and radical generations of ZrO<sub>2</sub> NPs exhibited better antimicrobial activity. The results indicate that ZrO<sub>2</sub> NPs are a possible candidate for the photocatalytic removal of toxic dye, pathogenic deactivators, and wastewater treatment. Moreover, the green method of ZrO<sub>2</sub> NPs production is found to be an alternative and effective method for the synthesis of NPs, and it is a more affirming method than other available methods.

**Author Contributions:** Conceptualization, P.C. and S.M.W.; methodology, P.C.; software, H.P.S. and H.S.M.; validation, P.C., A.I. and S.M.W.; formal analysis, P.C.; investigation, P.C.; re-sources, M.A.N., H.S.M., D.A.S., A.I., S.M.W. and W.-C.L.; data curation, A.I.; writing—original draft preparation, P.C.; writing—review and editing, P.C., S.M.W., A.I., W.-C.L. and D.A.S.; visualization, P.C.; supervision, P.C.; project administration, P.C.; funding acquisition, S.M.W. and W.-C.L. All authors have read and agreed to the published version of the manuscript.

**Funding:** The authors are grateful to the Researchers Supporting Project No. (RSP2023R448), King Saud University, Riyadh, Saudi Arabia.

**Institutional Review Board Statement:** Not applicable.

**Informed Consent Statement:** Not applicable.

**Data Availability Statement:** All research data are within the manuscript.

**Acknowledgments:** The authors are grateful to the Researchers Supporting Project No. (RSP2023R448), King Saud University, Riyadh, Saudi Arabia. Parvathiraja Chelliah draw the thanks to Indian Institute of Technology, Roorkee and Manipur University, Manipur, India.

**Conflicts of Interest:** The authors declare no conflict of interest.

## References

1. Ferreira, S.L.; da Silva Junior, J.B.; dos Santos, I.F.; de Oliveira, O.M.; Cerda, V.; Queiroz, A.F. Use of pollution indices and ecological risk in the assessment of contamination from chemical elements in soils and sediments—Practical aspects. *Trends Environ. Anal. Chem.* **2022**, *35*, e00169. [[CrossRef](#)]
2. Zerizghi, T.; Guo, Q.; Tian, L.; Wei, R.; Zhao, C. An integrated approach to quantify ecological and human health risks of soil heavy metal contamination around coal mining area. *Sci. Total Environ.* **2022**, *814*, 152653. [[CrossRef](#)]
3. Dan, S.F.; Udoh, E.C.; Wang, Q. Contamination and ecological risk assessment of heavy metals, and relationship with organic matter sources in surface sediments of the Cross River Estuary and nearshore areas. *J. Hazard. Mater.* **2022**, *438*, 129531. [[CrossRef](#)]
4. Barizon, R.R.M.; Kummrow, F.; de Albuquerque, A.F.; Assalin, M.R.; Rosa, M.A.; de Souza Dutra, D.R.C.; Pazianotto, R.A.A. Surface water contamination from pesticide mixtures and risks to aquatic life in a high-input agricultural region of Brazil. *Chemosphere* **2022**, *308*, 136400. [[CrossRef](#)]
5. Moloantoa, K.M.; Khetsha, Z.P.; Van Heerden, E.; Castillo, J.C.; Cason, E.D. Nitrate Water Contamination from Industrial Activities and Complete Denitrification as a Remediation Option. *Water* **2022**, *14*, 799. [[CrossRef](#)]
6. Schöenberger, U.T.; Simon, J.; Stamm, C. Are spray drift losses to agricultural roads more important for surface water contamination than direct drift to surface waters? *Sci. Total Environ.* **2022**, *809*, 151102. [[CrossRef](#)]
7. Bigot-Clivot, A.; La Carbona, S.; Cazeaux, C.; Durand, L.; Géba, E.; Le Foll, F.; Xuereb, B.; Chalghmi, H.; Dubey, J.P.; Bastien, F.; et al. Blue mussel (*Mytilus edulis*)—A bioindicator of marine water contamination by protozoa: Laboratory and in situ approaches. *J. Appl. Microbiol.* **2022**, *132*, 736–746. [[CrossRef](#)]
8. Lowe, B.; Gardy, J.; Wu, K.; Hassanpour, A. Mixed Metal Oxide Catalysts in Biodiesel Production. *Biodiesel Prod. Feedstocks Catal. Technol.* **2022**, *12*, 143–166.

9. Stoukatch, S.; Fagnard, J.F.; Dupont, F.; Laurent, P.; Debliquy, M.; Redouté, J.M. Low Thermal Conductivity Adhesive as a Key Enabler for Compact, Low-Cost Packaging for Metal-Oxide Gas Sensors. *IEEE Access* **2022**, *10*, 19242–19253. [[CrossRef](#)]
10. Wang, H.; Biswas, P.; Zachariah, M.R. Direct Imaging and Simulation of the Interface Reaction of Metal/Metal Oxide Nanoparticle Laminates. *J. Phys. Chem. C* **2022**, *126*, 8684–8691. [[CrossRef](#)]
11. Bielsa, D.; Oregui, M.; Arias, P.L. New insights into Mn<sub>2</sub>O<sub>3</sub> based metal oxide granulation technique with enhanced chemical and mechanical stability for thermochemical energy storage in packed bed reactors. *Sol. Energy* **2022**, *241*, 248–261. [[CrossRef](#)]
12. Hashemi, S.M.; Mohamedali, M.; Sedghkarder, M.H.; Mahinpey, N. Stability of CaO-based Sorbents under Realistic Calcination Conditions: Effect of Metal Oxide Supports. *ACS Sustain. Chem. Eng.* **2022**, *10*, 9760–9769. [[CrossRef](#)]
13. Fatimah, I.; Fadillah, G.; Yanti, I.; Doong, R.A. Clay-Supported Metal Oxide Nanoparticles in Catalytic Advanced Oxidation Processes: A Review. *Nanomaterials* **2022**, *12*, 825. [[CrossRef](#)] [[PubMed](#)]
14. Tran, T.V.; Nguyen, D.T.C.; Kumar, P.S.; Din, A.T.M.; Jalil, A.A.; Vo, D.V.N. Green synthesis of ZrO<sub>2</sub> NPs and nanocomposites for biomedical and environmental applications: A review. *Environ. Chem. Lett.* **2022**, *20*, 1309–1331. [[CrossRef](#)] [[PubMed](#)]
15. Chęcińska, K.; Chęciński, M.; Sikora, M.; Nowak, Z.; Karwan, S.; Chlubek, D. The Effect of Zirconium Dioxide (ZrO<sub>2</sub>) Nanoparticles Addition on the Mechanical Parameters of Polymethyl Methacrylate (PMMA): A Systematic Review and Meta-Analysis of Experimental Studies. *Polymers* **2022**, *14*, 1047. [[CrossRef](#)]
16. Aati, S.; Shrestha, B.; Fawzy, A. Cytotoxicity and antimicrobial efficiency of ZrO<sub>2</sub> NPs reinforced 3D printed resins. *Dent. Mater.* **2022**, *38*, 1432–1442. [[CrossRef](#)]
17. Chen, Y.; Yang, G.; Liu, B.; Kong, H.; Xiong, Z.; Guo, L.; Wei, G. Biomineralization of ZrO<sub>2</sub> NPs on graphene oxide-supported peptide/cellulose binary nanofibrous membranes for high-performance removal of fluoride ions. *Chem. Eng. J.* **2022**, *430*, 132721. [[CrossRef](#)]
18. Peng, S.; Li, R.; Huang, Y.; Zhang, Y.; Cao, J.J.; Lee, S. Interfacial dependent reactive oxygen species generation over Pt-ZrO<sub>2</sub> NPs for catalytic oxidation of formaldehyde at room temperature. *Appl. Surf. Sci.* **2022**, *600*, 154056. [[CrossRef](#)]
19. Alagarsamy, A.; Chandrasekaran, S.; Manikandan, A. Green synthesis and characterization studies of biogenic zirconium oxide (ZrO<sub>2</sub>) nanoparticles for adsorptive removal of methylene blue dye. *J. Mol. Struct.* **2022**, *1247*, 131275. [[CrossRef](#)]
20. Xavier, J.R. Electrochemical and dynamic mechanical properties of polyurethane nanocomposite reinforced with functionalized TiO<sub>2</sub>-ZrO<sub>2</sub> NPs in automobile industry. *Appl. Nanosci.* **2022**, *12*, 1763–1778. [[CrossRef](#)]
21. Li, N.; Yu, N.; Yi, Z.; An, D.; Xie, Z. CeO<sub>2</sub>-stabilised ZrO<sub>2</sub> NPs with excellent sintering performances synthesized by sol-gel-flux method. *J. Eur. Ceram. Soc.* **2022**, *42*, 1645–1655. [[CrossRef](#)]
22. Li, N.; An, D.; Yi, Z.; Yu, N.; Xie, Z. Synthesis of 1Y6Ce-ZrO<sub>2</sub> NPs with excellent sintering performance via novel Sol-Gel-Flux method. *Ceram. Int.* **2022**, *48*, 2637–2644. [[CrossRef](#)]
23. Chen, X.; Huang, G.; An, C.; Feng, R.; Wu, Y.; Huang, C. Superwetting polyethersulfone membrane functionalized with ZrO<sub>2</sub> NPs for polycyclic aromatic hydrocarbon removal. *J. Mater. Sci. Technol.* **2022**, *98*, 14–25. [[CrossRef](#)]
24. Sagadevan, S.; Imteyaz, S.; Murugan, B.; Lett, J.A.; Sridewi, N.; Weldegebrieal, G.K.; Fatimah, I.; Oh, W.C. A comprehensive review on green synthesis of titanium dioxide nanoparticles and their diverse biomedical applications. *Green Process. Synth.* **2022**, *11*, 44–63. [[CrossRef](#)]
25. Manikandan, V.; Lee, N.Y. Green synthesis of carbon quantum dots and their environmental applications. *Environ. Res.* **2022**, *212*, 113283. [[CrossRef](#)]
26. Prakash, M.; Kavitha, H.P.; Abinaya, S.; Vennila, J.P.; Lohita, D. Green synthesis of bismuth based nanoparticles and its applications-A review. *Sustain. Chem. Pharm.* **2022**, *25*, 100547. [[CrossRef](#)]
27. Tan, M.A.; Sharma, N.; An, S.S.A. Multi-Target Approach of *Murraya koenigii* Leaves in Treating Neurodegenerative Diseases. *Pharmaceuticals* **2022**, *15*, 188. [[CrossRef](#)]
28. Elamin, N.Y.; Indumathi, T.; Kumar, E.R. *Murraya koenigii* mediated synthesis of cobalt doped NiO nanoparticles: Evaluation of structural, optical properties and anti-bacterial activity. *Phys. E Low-Dimens. Syst. Nanostructures* **2022**, *142*, 115295. [[CrossRef](#)]
29. Bhatt, S.; Dadwal, V.; Padwad, Y.; Gupta, M. Study of physicochemical, nutritional, and anticancer activity of *Murraya Koenigii* extract for its fermented beverage. *J. Food Process. Preserv.* **2022**, *46*, e16137. [[CrossRef](#)]
30. Nur, A.S.; Sultana, M.; Mondal, A.; Islam, S.; Robel, F.N.; Islam, M.A.; Sumi, M.S.A. A review on the development of elemental and codoped TiO<sub>2</sub> photocatalysts for enhanced dye degradation under UV-vis irradiation. *J. Water Process Eng.* **2022**, *47*, 102728. [[CrossRef](#)]
31. Shah, P.; Unnarkat, A.; Patel, F.; Shah, M.; Shah, P. A comprehensive review on spinel based novel catalysts for visible light assisted dye degradation. *Process Saf. Environ. Prot.* **2022**, *161*, 703–722. [[CrossRef](#)]
32. Liu, Q.; Zhai, D.; Xiao, Z.; Tang, C.; Sun, Q.; Bowen, C.R.; Luo, H.; Zhang, D. Piezo-photoelectronic coupling effect of BaTiO<sub>3</sub>@TiO<sub>2</sub> nanowires for highly concentrated dye degradation. *Nano Energy* **2022**, *92*, 106702. [[CrossRef](#)]
33. Xie, K.; Wei, S.; Alhadhrani, A.; Liu, J.; Zhang, P.; Elnaggar, A.Y.; Zhang, F.; Mahmoud, M.H.H.; Murugadoss, V.; El-Bahy, S.M.; et al. Synthesis of CsPbBr<sub>3</sub>/CsPb<sub>2</sub>Br<sub>5</sub>@silica yolk-shell composite microspheres: Precisely controllable structure and improved catalytic activity for dye degradation. *Adv. Compos. Hybrid Mater.* **2022**, *5*, 1423–1432. [[CrossRef](#)]
34. Shah, P.; Joshi, K.; Shah, M.; Unnarkat, A.; Patel, F.J. Photocatalytic dye degradation using nickel ferrite spinel and its nanocomposite. *Environ. Sci. Pollut. Res.* **2022**, *29*, 78255–78264. [[CrossRef](#)] [[PubMed](#)]
35. Mansoorianfar, M.; Shahin, K.; Hojjati-Najafabadi, A.; Pei, R. MXene-laden bacteriophage: A new antibacterial candidate to control bacterial contamination in water. *Chemosphere* **2022**, *290*, 133383. [[CrossRef](#)]

36. Fonseca, S.; Cayer, M.P.; Ahmmed, K.T.; Khadem-Mohtaram, N.; Charette, S.J.; Brouard, D. Characterization of the Antibacterial Activity of an SiO<sub>2</sub> Nanoparticulate Coating to Prevent Bacterial Contamination in Blood Products. *Antibiotics* **2022**, *11*, 107. [[CrossRef](#)]
37. Verhorstert, K.W.; Riool, M.; Bulten, T.; Guler, Z.; de Boer, L.; Roovers, J.P.W.; Zaat, S.A. The impact of bacterial contamination on the host response towards fully absorbable poly-4-hydroxybutyrate and nonabsorbable polypropylene pelvic floor implants. *Mater. Today Bio* **2022**, *15*, 100268. [[CrossRef](#)]
38. Saadi, S.; Allem, R.; Sebahia, M.; Merouane, A.; Bakkali, M. Bacterial contamination of neglected hospital surfaces and equipment in an Algerian hospital: An important source of potential infection. *Int. J. Environ. Health Res.* **2022**, *32*, 1373–1381. [[CrossRef](#)]
39. Bermond, C.; Cherrad, S.; Trainoy, A.; Ngari, C.; Poulet, V. Real-time qPCR to evaluate bacterial contamination of cosmetic cream and the efficiency of protective ingredients. *J. Appl. Microbiol.* **2022**, *132*, 2106–2120. [[CrossRef](#)]
40. Thaler, M.; Khosravi, I.; Lechner, R.; Ladner, B.; Coraça-Huber, D.C.; Nogler, M. An intraoperative assessment of bacterial contamination on surgical helmets and gloves during arthroplasty surgeries. *HIP Int.* **2022**, *32*, 426–430. [[CrossRef](#)]
41. Sharmila, M.; Mani, R.J.; Parvathiraja, C.; Kader, S.M.A.; Siddiqui, M.R.; Wabaidur, S.M.; Islam, M.A.; Lai, W.-C. Photocatalytic Dye Degradation and Bio-Insights of Honey-Produced  $\alpha$ -Fe<sub>2</sub>O<sub>3</sub> Nanoparticles. *Water* **2022**, *14*, 2301. [[CrossRef](#)]
42. Parvathiraja, C.; Katheria, S.; Siddiqui, M.R.; Wabaidur, S.M.; Islam, M.A.; Lai, W.C. Activated Carbon-Loaded Titanium Dioxide Nanoparticles and Their Photocatalytic and Antibacterial Investigations. *Catalysts* **2022**, *12*, 834. [[CrossRef](#)]
43. Balakrishnan, R.; Vijayaraja, D.; Jo, S.H.; Ganesan, P.; Su-Kim, I.; Choi, D.K. Medicinal profile, phytochemistry, and pharmacological activities of *Murraya koenigii* and its primary bioactive compounds. *Antioxidants* **2020**, *9*, 101. [[CrossRef](#)] [[PubMed](#)]
44. Abuga, I.; Sulaiman, S.F.; Wahab, R.A.; Ooi, K.L.; Rasad, M.S.B.A. In vitro antibacterial effect of the leaf extract of *Murraya koenigii* on cell membrane destruction against pathogenic bacteria and phenolic compounds identification. *Eur. J. Integr. Med.* **2020**, *33*, 101010. [[CrossRef](#)]
45. Alam, M.N.; Das, S.; Batuta, S.; Roy, N.; Chatterjee, A.; Mandal, D.; Begum, N.A. *Murraya koenigii* Spreng. leaf extract: An efficient green multifunctional agent for the controlled synthesis of Au nanoparticles. *ACS Sustain. Chem. Eng.* **2014**, *2*, 652–664. [[CrossRef](#)]
46. Reddy, C.V.; Reddy, K.R.; Shim, J.; Aminabhavi, T.M. Synthesis of transition metal ions doped-ZrO<sub>2</sub> NPs supported g-C<sub>3</sub>N<sub>4</sub> hybrids for solar light-induced photocatalytic removal of methyl orange and tetracycline pollutants. *Chemosphere* **2022**, *308*, 136414. [[CrossRef](#)]
47. Diao, F.; Wang, C.; Qiu, L.; Yin, Y.; Zhao, F.; Chang, H. Interaction between Nickel Oxide and Support Promotes Selective Catalytic Reduction of NO<sub>x</sub> with C<sub>3</sub>H<sub>6</sub>. *Chem. Asian J.* **2022**, *17*, e202200520. [[CrossRef](#)]
48. Singh, A.; Goyal, V.; Singh, J.; Kaur, H.; Kumar, S.; Batoor, K.M.; Gaur, J.; Pal, M.; Rawat, M.; Hussain, S. Structurally and morphologically engineered single-pot biogenic synthesis of NiO nanoparticles with enhanced photocatalytic and antimicrobial activities. *J. Clean. Prod.* **2022**, *343*, 131026. [[CrossRef](#)]
49. Das, R.S.; Warkhade, S.K.; Kumar, A.; Wankhade, A.V. Graphene oxide-based zirconium oxide nanocomposite for enhanced visible light-driven photocatalytic activity. *Res. Chem. Intermed.* **2019**, *45*, 1689–1705. [[CrossRef](#)]
50. Zhou, S.; Garnweitner, G.; Niederberger, M.; Antonietti, M. Dispersion behavior of zirconia nanocrystals and their surface functionalization with vinyl group-containing ligands. *Langmuir* **2007**, *23*, 9178–9187. [[CrossRef](#)]
51. Sidhu, G.K.; Kaushik, A.K.; Rana, S.; Bhansali, S.; Kumar, R. Photoluminescence quenching of Zirconia nanoparticle by surface modification. *Appl. Surf. Sci.* **2015**, *334*, 216–221. [[CrossRef](#)]
52. Waris, A.; Din, M.; Ali, A.; Ali, M.; Afridi, S.; Baset, A.; Khan, A.U. A comprehensive review of green synthesis of copper oxide nanoparticles and their diverse biomedical applications. *Inorg. Chem. Commun.* **2021**, *123*, 108369. [[CrossRef](#)]
53. Ahmad, W.; Kumar Jaiswal, K.; Amjad, M. *Euphorbia herita* leaf extract as a reducing agent in a facile green synthesis of iron oxide nanoparticles and antimicrobial activity evaluation. *Inorg. Nano-Met. Chem.* **2021**, *51*, 1147–1154. [[CrossRef](#)]
54. Lakshminarayanan, S.; Shereen, M.F.; Niraimathi, K.L.; Brindha, P.; Arumugam, A. One-pot green synthesis of iron oxide nanoparticles from *Bauhinia tomentosa*: Characterization and application towards synthesis of 1, 3 diolein. *Sci. Rep.* **2021**, *11*, 8643. [[CrossRef](#)] [[PubMed](#)]
55. Howell, I.R.; Einck, V.J.; Nees, D.; Stadlober, B.; Watkins, J.J. Solvent-free, transparent, high-refractive index ZrO<sub>2</sub> nanoparticle composite resin for scalable roll to roll UV-nanoimprint lithography. *Opt. Laser Technol.* **2021**, *141*, 107101. [[CrossRef](#)]
56. Higashino, M.; Murai, S.; Lo, T.Y.; Tomita, S.; Tanaka, K. Photoluminescence coupled to electric and magnetic surface lattice resonance in periodic arrays of zirconia nanoparticles. *J. Mater. Chem. C* **2022**, *10*, 9730–9739. [[CrossRef](#)]
57. Renuka, L.; Anantharaju, K.S.; Sharma, S.C.; Nagaswarupa, H.P.; Prashantha, S.C.; Nagabhushana, H.; Vidya, Y.S. Self-assembled hierarchical microporous ZrO<sub>2</sub> NPs and Mg-doped ZrO<sub>2</sub> nanodiscs synthesized by non-aqueous sol-gel route. *J. Mater. Sci. Mater. Electron.* **2022**, *672*, 609–622.
58. Kianfar, A.H.; Arayesh, M.A.; Momeni, M.M. Degradation of MB and RhB by modified ZrO<sub>2</sub> NPs via sunlight. *Appl. Phys. A* **2021**, *127*, 158. [[CrossRef](#)]
59. Goyal, P.; Bhardwaj, A.; Mehta, B.K.; Mehta, D. Research article green synthesis of zirconium oxide nanoparticles (ZrO<sub>2</sub>NPs) using *Helianthus annuus* seed and their antimicrobial effects. *J. Indian Chem. Soc.* **2021**, *98*, 100089. [[CrossRef](#)]
60. Sikdar, S.; Banu, A.; Ali, S.; Barman, S.; Kalar, P.L.; Das, R. Micro-structural Analysis and Photocatalytic Properties of Green Synthesized t-ZrO<sub>2</sub> NPs. *ChemistrySelect* **2022**, *7*, e202103953. [[CrossRef](#)]

61. Ahmed, T.; Ren, H.; Noman, M.; Shahid, M.; Liu, M.; Ali, M.A.; Zhang, J.; Tian, Y.; Qi, X. Green synthesis and characterization of zirconium oxide nanoparticles by using a native *Enterobacter* sp. and its antifungal activity against bayberry twig blight disease pathogen *Pestalotiopsis versicolor*. *NanoImpact* **2021**, *21*, 100281. [[CrossRef](#)] [[PubMed](#)]
62. Gurav, R.P.; Nalawade, R.D.; Sawant, S.D.; Satyanarayan, N.D.; Sankpal, S.A.; Hangirgekar, S.P. Biosynthesis of ZrO<sub>2</sub> for ZrO<sub>2</sub>@ Ag-S-CH<sub>2</sub>COOH as the retrievable catalyst for the one-pot green synthesis of pyrazoline derivatives and their anticancer evaluation. *Appl. Organomet. Chem.* **2022**, *36*, e6666. [[CrossRef](#)]
63. Hao, W.; Jia, Y.; Wang, C.; Wang, X. Preparation, chemical characterization and determination of the antioxidant, cytotoxicity and therapeutic effects of gold nanoparticles green-synthesized by *Calendula officinalis* flower extract in diabetes-induced cardiac dysfunction in rat. *Inorg. Chem. Commun.* **2022**, *144*, 109931. [[CrossRef](#)]
64. Govindasamy, R.; Govindarasu, M.; Alharthi, S.S.; Mani, P.; Bernaurdshaw, N.; Gomathi, T.; Ansari, M.A.; Alomary, M.N.; Atwah, B.; Malik, M.S.; et al. Sustainable green synthesis of yttrium oxide (Y<sub>2</sub>O<sub>3</sub>) nanoparticles using *Lantana camara* leaf extracts: Physicochemical characterization, photocatalytic degradation, antibacterial, and anticancer potency. *Nanomaterials* **2022**, *12*, 2393. [[CrossRef](#)]
65. Gonçalves, J.P.Z.; Seraglio, J.; Macuvele, D.L.P.; Padoin, N.; Soares, C.; Riella, H.G. Green synthesis of manganese based nanoparticles mediated by *Eucalyptus robusta* and *Corymbia citriodora* for agricultural applications. *Colloids Surf. A Physicochem. Eng. Asp.* **2022**, *636*, 128180. [[CrossRef](#)]
66. Vinayagam, R.; Singhania, B.; Murugesan, G.; Kumar, P.S.; Bhole, R.; Narasimhan, M.K.; Varadavenkatesan, T.; Selvaraj, R. Photocatalytic degradation of methylene blue dye using newly synthesized zirconia nanoparticles. *Environ. Res.* **2022**, *214*, 113785. [[CrossRef](#)]
67. Amirabad, T.N.; Ensafi, A.A.; Rezaei, B. Boosting supercapacitor performance by in-situ modification of binder-free electrodes with green synthesized Zn-doped Fe<sub>2</sub>O<sub>3</sub> nanoparticles on 2D-MoS<sub>2</sub>@ rGO nanosheets. *Fuel* **2022**, *330*, 125645. [[CrossRef](#)]
68. Guo, P.P.; He, Z.H.; Yang, S.Y.; Wang, W.; Wang, K.; Li, C.C.; Wei, Y.-Y.; Liu, Z.-T.; Han, B. Electrocatalytic CO<sub>2</sub> reduction to ethylene over ZrO<sub>2</sub>/Cu-Cu<sub>2</sub>O catalysts in aqueous electrolytes. *Green Chem.* **2022**, *24*, 1527–1533. [[CrossRef](#)]
69. Zhang, L.; Han, J.; Wang, Y.; Yang, W.; Tao, S. Pd/Mg(OH)<sub>2</sub>/MgO-ZrO<sub>2</sub> Nanocomposite Systems for Highly Efficient Suzuki-Miyaura Coupling Reaction at Room Temperature: Implications for Low-Carbon Green Organic Synthesis. *ACS Appl. Nano Mater.* **2022**, *5*, 8059–8069. [[CrossRef](#)]
70. Tsegay, M.G.; Gebretinsae, H.G.; Welegergs, G.G.; Maaza, M.; Nuru, Z.Y. Novel green synthesized Cr<sub>2</sub>O<sub>3</sub> for selective solar absorber: Investigation of structural, morphological, chemical, and optical properties. *Sol. Energy* **2022**, *236*, 308–319. [[CrossRef](#)]
71. Lin, Y.; Jin, X.; Khan, N.I.; Owens, G.; Chen, Z. Bimetallic Fe/Ni nanoparticles derived from green synthesis for the removal of arsenic (V) in mine wastewater. *J. Environ. Manag.* **2022**, *301*, 113838. [[CrossRef](#)] [[PubMed](#)]
72. Gan, L.; Xu, L.; Shang, S.; Zhou, X.; Meng, L. Visible light induced methylene blue dye degradation photo-catalyzed by WO<sub>3</sub>/graphene nanocomposites and the mechanism. *Ceram. Int.* **2016**, *42*, 15235–15241. [[CrossRef](#)]
73. Rajkumar, M.; Arunpandian, M.; Leeladevi, K.; Veemaraj, T.; Arunachalam, S. Construction of novel Bi<sub>2</sub>MoO<sub>6</sub>@ V<sub>2</sub>O<sub>5</sub> nanocomposite as visible-light-driven catalyst for degradation of methylene blue dye. *J. Mater. Sci. Mater. Electron.* **2022**, *33*, 5816–5830. [[CrossRef](#)]
74. Perumal, V.; Inmozhi, C.; Uthrakumar, R.; Robert, R.; Chandrasekar, M.; Mohamed, S.B.; Honey, S.; Raja, A.; Al-Mekhlafi, F.A.; Kaviyarasu, K. Enhancing the photocatalytic performance of surface-Treated SnO<sub>2</sub> hierarchical nanorods against methylene blue dye under solar irradiation and biological degradation. *Environ. Res.* **2022**, *209*, 112821. [[CrossRef](#)]
75. Belousov, A.S.; Suleimanov, E.V.; Parkhacheva, A.A.; Fukina, D.G.; Koryagin, A.V.; Koroleva, A.V.; Zhizhin, E.V.; Gorshkov, A.P. Regulating of MnO<sub>2</sub> photocatalytic activity in degradation of organic dyes by polymorphic engineering. *Solid State Sci.* **2022**, *132*, 106997. [[CrossRef](#)]
76. Kumar, S.A.; Jarvin, M.; Inbanathan, S.S.R.; Umar, A.; Lalla, N.P.; Dzade, N.Y.; Algadi, H.; Rahman, Q.I.; Baskoutas, S. Facile green synthesis of magnesium oxide nanoparticles using tea (*Camellia sinensis*) extract for efficient photocatalytic degradation of methylene blue dye. *Environ. Technol. Innov.* **2022**, *28*, 102746. [[CrossRef](#)]
77. Koyyada, G.; Goud, B.S.; Devarayapalli, K.C.; Shim, J.; Vattikuti, S.P.; Kim, J.H. BiFeO<sub>3</sub>/Fe<sub>2</sub>O<sub>3</sub> electrode for photoelectrochemical water oxidation and photocatalytic dye degradation: A single step synthetic approach. *Chemosphere* **2022**, *303*, 135071. [[CrossRef](#)]
78. Sugashini, S.; Gomathi, T.; Devi, R.A.; Sudha, P.N.; Rambabu, K.; Banat, F. Nanochitosan/carboxymethyl cellulose/TiO<sub>2</sub> biocomposite for visible-light-induced photocatalytic degradation of crystal violet dye. *Environ. Res.* **2022**, *204*, 112047. [[CrossRef](#)]
79. Aravinthkumar, K.; Peter, I.J.; Babu, G.A.; Navaneethan, M.; Karazhanov, S.; Mohan, C.R. Enhancing the short circuit current of a Dye-Sensitized Solar cell and photocatalytic dye degradation using Cr doped SrTiO<sub>3</sub> interconnected spheres. *Mater. Lett.* **2022**, *319*, 132284. [[CrossRef](#)]
80. Noor, M.; Sharmin, F.; Al Mamun, M.A.; Hasan, S.; Hakim, M.A.; Basith, M.A. Effect of Gd and Y co-doping in BiVO<sub>4</sub> photocatalyst for enhanced degradation of methylene blue dye. *J. Alloy. Compd.* **2022**, *895*, 162639. [[CrossRef](#)]
81. George, A.; Magimai Antoni Raj, D.; Venci, X.; Dhayal Raj, A.; Albert Irudayaraj, A.; Josephine, R.L.; John Sundaram, S.; Al-Mohaimeed, A.M.; Al Farraj, D.A.; Chen, T.W.; et al. Photocatalytic effect of CuO nanoparticles flower-like 3D nanostructures under visible light irradiation with the degradation of methylene blue (MB) dye for environmental application. *Environ. Res.* **2022**, *203*, 111880. [[CrossRef](#)] [[PubMed](#)]
82. Qutub, N.; Singh, P.; Sabir, S.; Sagadevan, S.; Oh, W.C. Enhanced photocatalytic degradation of Acid Blue dye using CdS/TiO<sub>2</sub> nanocomposite. *Sci. Rep.* **2022**, *12*, 5759. [[CrossRef](#)] [[PubMed](#)]

83. Agorku, E.S.; Kuvarega, A.T.; Mamba, B.B.; Pandey, A.C.; Mishra, A.K. Enhanced visible-light photocatalytic activity of multi-elements-doped ZrO<sub>2</sub> for degradation of indigo carmine. *J. Rare Earths* **2015**, *33*, 498–506. [[CrossRef](#)]
84. Hanafi, M.F.; Sapawe, N. The potential of ZrO<sub>2</sub> catalyst toward degradation of dyes and phenolic compound. *Mater. Today Proc.* **2019**, *19*, 1524–1528. [[CrossRef](#)]
85. Khataee, A.; Kayan, B.; Gholami, P.; Kalderis, D.; Akay, S.; Dinpazhoh, L. Sonocatalytic degradation of Reactive Yellow 39 using synthesized ZrO<sub>2</sub> NPs on biochar. *Ultrason. Sonochemistry* **2017**, *39*, 540–549. [[CrossRef](#)]
86. Reddy, C.V.; Babu, B.; Reddy, I.N.; Shim, J. Synthesis and characterization of pure tetragonal ZrO<sub>2</sub> NPs with enhanced photocatalytic activity. *Ceram. Int.* **2018**, *44*, 6940–6948. [[CrossRef](#)]
87. Renuka, L.; Anantharaju, K.S.; Sharma, S.C.; Nagabhushana, H.; Vidya, Y.S.; Nagaswarupa, H.P.; Prashantha, S.C. A comparative study on the structural, optical, electrochemical and photocatalytic properties of ZrO<sub>2</sub> nanooxide synthesized by different routes. *J. Alloy. Compd.* **2017**, *695*, 382–395. [[CrossRef](#)]
88. Dharr, A.; Arjun, A.; Raguram, T.; Rajni, K.S. Influence of pH on the structural, spectral, optical, morphological and photocatalytic properties of ZrO<sub>2</sub> NPs synthesized by sol–gel technique. *J. Mater. Sci. Mater. Electron.* **2020**, *31*, 15718–15730. [[CrossRef](#)]
89. Karthik, K.; Madhukara Naik, M.; Shashank, M.; Vinuth, M.; Revathi, V. Microwave-assisted ZrO<sub>2</sub> NPs and its photocatalytic and antibacterial studies. *J. Clust. Sci.* **2019**, *30*, 311–318. [[CrossRef](#)]
90. Basahel, S.N.; Ali, T.T.; Mokhtar, M.; Narasimharao, K. Influence of crystal structure of nanosized ZrO<sub>2</sub> on photocatalytic degradation of methyl orange. *Nanoscale Res. Lett.* **2015**, *10*, 73. [[CrossRef](#)]
91. Sreethawong, T.; Ngamsinlapasathian, S.; Yoshikawa, S. Synthesis of crystalline mesoporous-assembled ZrO<sub>2</sub> NPs via a facile surfactant-aided sol–gel process and their photocatalytic dye degradation activity. *Chem. Eng. J.* **2013**, *228*, 256–262. [[CrossRef](#)]
92. Rizwana, H.; Alwhibi, M.S.; Al-Judaie, R.A.; Aldehaish, H.A.; Alsaggabi, N.S. Sunlight-mediated green synthesis of silver nanoparticles using the berries of Ribes rubrum (*Red currants*): Characterisation and evaluation of their antifungal and antibacterial activities. *Molecules* **2022**, *27*, 2186. [[CrossRef](#)] [[PubMed](#)]
93. Prema, P.; Ranjani, S.S.; Kumar, K.R.; Veeramanikandan, V.; Mathiyazhagan, N.; Nguyen, V.H.; Balaji, P. Microbial synthesis of silver nanoparticles using *Lactobacillus plantarum* for antioxidant, antibacterial activities. *Inorg. Chem. Commun.* **2022**, *136*, 109139. [[CrossRef](#)]
94. Nieto-Maldonado, A.; Bustos-Guadarrama, S.; Espinoza-Gomez, H.; Flores-López, L.Z.; Ramirez-Acosta, K.; Alonso-Nuñez, G.; Cadena-Nava, R.D. Green synthesis of copper nanoparticles using different plant extracts and their antibacterial activity. *J. Environ. Chem. Eng.* **2022**, *10*, 107130. [[CrossRef](#)]
95. Dai, X.; Li, S.; Li, S.; Ke, K.; Pang, J.; Wu, C.; Yan, Z. High antibacterial activity of chitosan films with covalent organic frameworks immobilized silver nanoparticles. *Int. J. Biol. Macromol.* **2022**, *202*, 407–417. [[CrossRef](#)]
96. Gevorgyan, S.; Schubert, R.; Falke, S.; Lorenzen, K.; Trchounian, K.; Betzel, C. Structural characterization and antibacterial activity of silver nanoparticles synthesized using a low-molecular-weight Royal Jelly extract. *Sci. Rep.* **2022**, *12*, 14077. [[CrossRef](#)]
97. Al Hagbani, T.; Rizvi, S.M.D.; Hussain, T.; Mehmood, K.; Rafi, Z.; Moin, A.; Abu Lila, A.S.; Alshammari, F.; Khafagy, E.S.; Rahamathulla, M.; et al. Cefotaxime Mediated Synthesis of Gold Nanoparticles: Characterization and Antibacterial Activity. *Polymers* **2022**, *14*, 771. [[CrossRef](#)]
98. Nazari-pour, E.; Mosazadeh, F.; Rahimi, S.S.; Alijani, H.Q.; Isaei, E.; Borhani, F.; Iravani, S.; Ghasemi, M.; Akbarizadeh, M.R.; Khatami, M.; et al. Ferromagnetic nickel (II) oxide (NiO) nanoparticles: Biosynthesis, characterization and their antibacterial activities. *Rend. Lincei. Sci. Fis. E Nat.* **2022**, *33*, 127–134. [[CrossRef](#)]
99. Guo, C.; Cheng, F.; Liang, G.; Zhang, S.; Jia, Q.; He, L.; Duan, S.; Fu, Y.; Zhang, Z.; Du, M. Copper-based polymer-metal–organic framework embedded with Ag nanoparticles: Long-acting and intelligent antibacterial activity and accelerated wound healing. *Chem. Eng. J.* **2022**, *435*, 134915. [[CrossRef](#)]
100. Naveen, K.V.; Kim, H.Y.; Saravanakumar, K.; Mariadoss, A.V.A.; Wang, M.H. Phyto-fabrication of biocompatible silver nanoparticles using *Potentilla chinensis* Ser leaves: Characterization and evaluation of its antibacterial activity. *J. Nanostructure Chem.* **2022**, *12*, 655–667. [[CrossRef](#)]
101. Rao, S.Q.; Zhang, R.Y.; Chen, R.; Gao, Y.J.; Gao, L.; Yang, Z.Q. Nanoarchitectonics for enhanced antibacterial activity with *Lactobacillus buchneri* S-layer proteins-coated silver nanoparticles. *J. Hazard. Mater.* **2022**, *426*, 128029. [[CrossRef](#)] [[PubMed](#)]

**Disclaimer/Publisher’s Note:** The statements, opinions and data contained in all publications are solely those of the individual author(s) and contributor(s) and not of MDPI and/or the editor(s). MDPI and/or the editor(s) disclaim responsibility for any injury to people or property resulting from any ideas, methods, instructions or products referred to in the content.